Synthesis of amino acid functionalized Fe_3O_4 nanoparticles for adsorptive removal of Rhodamine B

Neway Belachew[1] · Aschalew Tadesse[2] · Mebrahtu Hagos Kahsay[3] · Desta Shumuye Meshesha[4] · Keloth Basavaiah[5]

Abstract

L-Aspartic acid (L-Asp) functionalized magnetite nanoparticles (Fe_3O_4 NPs) were synthesized through a facile co-precipitation method using L-Asp as a capping agent. UV–Vis, FTIR, XRD, SEM, EDS, TEM, and VSM techniques were used to investigate the formation, morphology, elemental composition, and magnetic properties of the synthesized Fe_3O_4 NPs. Highly crystalline and spherical shaped pure phase Fe_3O_4 NPs were successfully synthesized using amino acid as a capping agent. The magnetic measurement analysis confirms the superparamagnetic nature of the synthesized L-Asp capped Fe_3O_4 NPs. The adsorption efficiency of L-Asp capped Fe_3O_4 NPs was assessed by the removal of Rhodamine B (RhB). The optimum removal efficiency was found to be 7.7 mg g^{-1} using 1 mg mL^{-1} adsorbent, and 30 mg L^{-1} RhB at pH 7 and 25 °C. The regression (R^2_{adj}) and standard deviation (SD) analysis were used to validate both kinetic and isotherm models. Avrami fractional-order and Liu models were selected as the best kinetic and isotherms, respectively. The maximum adsorption capacity (Q_o) of L-Asp Fe_3O_4 NPs toward RhB Liu's model was found to be 10.44 mg g^{-1}.

Keywords Green synthesis · Magnetite nanoparticles · Amino acid · Capping agent · Rhodamine B

Introduction

Recently, water contamination due to numerous organic, inorganic, and biological pollutants has become a huge worldwide environmental issue. The presence of organic dyes in effluents can cause adverse effects to human health and marine organisms because of their toxicity,

carcinogenesis, mutagenesis, and teratogenesis (Alkaykh et al. 2020; Gupta et al. 2020). The massive discharge of dyes from various industries such as textiles, rubber, leather, paper, food, and pharmaceutical can interfere with the photosynthetic activities of the aquatic life by introducing high biochemical and chemical oxygen demands (BOD and COD), coloration, and toxicity to water (Kahsay et al. 2019; Belachew and Bekele 2020; Mohanraj et al. 2020). RhB is one of the commonest xanthine-based fluorescent dye widely used as a tracer dye, biomarker, and other industrial applications (Kooh et al. 2016). It is a cationic dye, highly soluble in water (8–15 g/L), and ethanol (15 g/L) (Chieng et al. 2015). However, the discharges of RhB to the water bodies have brought several anxieties to aquatic life and human health. It is carcinogenic and destructs both the eye and skin (Singh et al. 2020). Moreover, RhB due to its poor degradability under light irradiation and strong solubility in water (~ 15 g/L at 20 °C), it is difficult to remove by conventional water treatment techniques. Hence, it is highly desirable to develop an effective method for the removal of dyes from contaminated water below the acceptable threshold values before discharging them to the environment.

✉ Neway Belachew
neway.du@gmail.com; neway@dbu.edu.et

1 Department of Chemistry, Debre Berhan University, Debre Berhan, Ethiopia

2 Department of Chemistry, Adama Science and Technology University, Adama, Ethiopia

3 Department of Chemistry, Woldia University, Woldia, Ethiopia

4 Department of Chemistry, University of Gondar, Gondar, Ethiopia

5 Department of Inorganic and Analytical Chemistry, Andhra University, Vishakapatnam 530003, India

Many techniques have been developed for treatments of dye effluent including flocculation, coagulation, chemical precipitation, ozonation, adsorption, chemical oxidation, membrane filtration, bio and photocatalytic degradation (Rajasulochana and Preethy 2016; Belachew et al. 2017, 2020; Anwer et al. 2019; Kiwaan et al. 2020). Adsorption is one of the extensively used approaches for the removal of dyes because of its efficiency, simplicity, and relatively low cost (Dotto and McKay 2020). Numerous adsorbents such as clays, zeolites, activated carbon, and plant waste materials have been reported for the removal of dyes from wastewater (Belachew et al. 2016; Sellaoui et al. 2017; Kausar et al. 2018; Majid et al. 2019). However, the practical application of these adsorbents materials shows some limitations because of the high cost and low recoverability.

Recently, nanostructured materials have become attractive adsorbent materials for the efficient removal of water pollutants. They have a high surface-to-volume ratio and can easily modify their surface by introducing functional groups (Amin et al. 2014; Burakov et al. 2018). Fe_3O_4 NPs owing to biocompatibility, efficient adsorption capacity, and magnetic recoverability show promise for the removal of dyes from aqueous solutions (Gutierrez et al. 2017; Anjum et al. 2019; Gao 2019). Unfortunately, Fe_3O_4 NP has a strong magnetic dipole moment and large surface areas that are responsible for the irreversible agglomeration. Therefore, various surface modifying agents were used to overcome the agglomeration of Fe_3O_4 NPs. Lakouraj et al. (2015) have reported conducting polymer capped Fe_3O_4 NPs for cationic dye removal. Similarly, Shan et al. (2015) reported poly (methylmethacrylate-*co*-divinylbenzene) surface modified Fe_3O_4 NPs for RhB dye adsorption. Similarly, Keyhanian et al. (2016) were used sodium dodecyl sulfate (SDS) surfactant to modify the surface of Fe_3O_4 NPs for methyl violet dye adsorption. However, polymers, surfactants, and other organic compounds used for surface modification of Fe_3O_4 NPs are not environmentally benign. Hence, the syntheses of Fe_3O_4 NPs using greener reagents are desirable for practical applications. In this regard, environmentally friendly reagents such as phytochemical extracts, glucose, ascorbic acid, and amino acids have been used for the synthesis of Fe_3O_4 NPs. Amino acids owing to biocompatibility and interesting aqueous chemistry have taken a considerable interest. Amino acids are known by their active functional groups ($-COOH$ and NH_2) that help for surface modification of nanostructured materials (Schwaminger et al. 2015; Nosrati et al. 2018). In the current study, L-Aspartic acid was used as a capping agent for the modification of Fe_3O_4 NPs. L-Aspartic is a nonessential amino acid. To the best of our knowledge, there is no comprehensive report on the modification of Fe_3O_4 NPs for the removal of RhB.

In the present study, we report a facile and green synthesis of amino acid capped Fe_3O_4 NPs for the adsorptive removal of RhB dye. The nonlinear adsorption fitting was employed to investigate the kinetics and isotherms of RhB adsorption onto L-Asp capped Fe_3O_4 NPs.

Experimental

Materials

Iron (III) chloride hexahydrate ($FeCl_3 \cdot 6H_2O$) and iron (II) sulfate heptahydrate ($FeSO_4 \cdot 7H_2O$) used for the synthesis of Fe_3O_4 NPs were obtained from Merck, India. L-Aspartic acid was received from HiMedia, India. All other reagents were analytically graded and used without further purification. Milli-Q water was used throughout the whole synthesis process.

Synthesis of L-Aspartic acid capped Fe₃O₄ NPs

A facile co-precipitation method was used for the synthesis of Fe_3O_4 NPs in the presence of L-Asp as a capping and surface modifying agent. The aqueous solution of $FeCl_3 \cdot 6H_2O$ (0.54 g, 2×10^{-3} mol) and $FeSO_4 \cdot 7H_2O$ (0.278 g, 1×10^{-3} mol) in a 2:1 molar ratio was refluxed in 250 mL round-bottomed flask for 30 min at 70 ℃. Then, 5 mL ammonia solution (25%) in a drop-wise was added and continued the reaction for 1 h. Subsequently, L-Aspartic acid (5 mL, 2 M) as a surface modifying agent was added to the reaction mixture. The modification process was progressed for 2 h at 70 ℃ under constant stirring. Finally, the black precipitate was separated by an external magnet, washed several times with Milli-Q water, and then dried in the vacuum at room temperature. The same protocol was applied for the synthesis of uncapped Fe_3O_4 NPs in the absence of L-Asp.

Characterizations

The absorption spectra were recorded using UV–Visible spectrometer (Shimadzu 2450—SHIMADZU). Fourier transform-infrared (FTIR) spectra were recorded over the range of 400–4000 cm^{-1} using a SHIMADZU-IRPRESTIGE-2 Spectrometer. X-ray diffraction (XRD) patterns were recorded by PANalytical X'pert pro diffractometer at 0.02 degrees/sec scan rate using Cu-kα_1 radiation (1.5406 Å, 45 kV, 40 mA). Transmission electron microscopy images were obtained with the TEM model FEI TECNAI G2 S-Twin at an accelerating voltage of 120 and 200 kV. The morphologies of the samples were characterized by scanning electron microscopy (SEM, Zeiss Ultra-60) equipped with X-ray energy dispersive spectroscopy (EDS). Room temperature magnetization measurements versus applied magnetic fields were carried out using a vibrating sample magnetometer (VSM), Lakeshore 665, USA.

Batch mode adsorption studies

Batch adsorption efficiency of L-Asp capped Fe_3O_4 NPs was carried out at room temperature (25 °C) using RhB as a model dye. Typically, 50 mg of L-Asp capped Fe_3O_4 NP was mixed with 50 mL of known concentration of dye solution in a 250 mL Erlenmeyer flask. Three milliliters sample was withdrawn from each flask at the desired time of adsorption. The filtrate was separated by centrifugation and the absorbance of residual RhB dye in the solution was recorded at the $\lambda_{max} = 554$ nm. The adsorption capacity at equilibrium time, q (mg g^{-1}) of the adsorbent was determined by Eq. (1).

$$q = (C_o - C_t)V/m \tag{1}$$

where C_o is the initial concentration of RhB (mg L^{-1}), C_t is the concentration of RhB (mg L^{-1}) in solution at a time "t," V is the volume (L) of the aqueous solution, and m is the mass (g) of the adsorbent.

Adsorption kinetics

Kinetics of the adsorption process is helpful to investigate the rate, equilibrium time, and mass transfer mechanisms. Herein, adsorption kinetics of RhB onto L-Asp-Fe_3O_4 NPs was performed using 50 mg of adsorbent, 50 mL of 20 mg L^{-1} of adsorbate (RhB), and pH = 7. Pseudo-first order [Eq. (2)], pseudo-second-order [Eq. (3)], Avrami-Fractional-order [Eq. (4)], and Elovich [Eq. (5)] kinetic models were employed for fitting the kinetic data.

$$q_t = q_e(1 - \exp^{(-k_1 t)}) \tag{2}$$

$$q_t = \frac{k_2 q_e^2 t}{k_2 q_e t + 1} \tag{3}$$

$$q_t = q_e\left(1 - \exp\left(-(k_{AV} * t)\right)^{nAV}\right) \tag{4}$$

$$q_t = \frac{1}{a}\ln(1 + (a * b * t)) \tag{5}$$

where k_1 (min^{-1}), k_2 (g mg^{-1} min^{-1}), and k_{AV} (min^{-1}) are the rate constants for pseudo-first order, pseudo-second order, and Avrami fractional-order models, respectively. q_t and q_e in mg g^{-1} are the theoretical adsorption capacity at a time (t) and equilibrium time, respectively. C (mg g^{-1}) is a constant related to the thickness of the boundary layer. n_{AV} is a fractional reaction order of Avrami model. "a" is the initial velocity due to dq/dt with $q_t = 0$ (mg g^{-1} min^{-1}), and "b" is the desorption constant of the Elovich model (g mg^{-1}).

Adsorption isotherms models

The adsorption isotherm studies provide information about the equilibrium adsorption capacity of the adsorbent and plausible interaction between the adsorbate and adsorbent. The equilibrium isotherm process was performed for 120 min contact time by using 50 mg of L-Asp-Fe_3O_4 NPs, 50 mL of various concentrations of RhB ranging from 5 mg L^{-1} to 30 mg L^{-1} at pH 7. The Langmuir [Eq. (6)], Freundlich [Eq. (7)], and Liu [Eq. (8)] adsorption models were used to investigate the equilibrium data.

$$q_e = \frac{Q_{max}K_L C_e}{1 + K_L C_e} \tag{6}$$

$$q_e = K_F C_e^{1/n_F} \tag{7}$$

$$q_e = \frac{Q_{max}\left(K_g C_e\right)^{n_L}}{1 + \left(K_g C_e\right)^{n_L}} \tag{8}$$

where q_e (mg g^{-1}) and c_e (mg L^{-1}) are equilibrium adsorption capacity of adsorbent and the residual concentration of RhB at equilibrium, respectively; Q_{max} is the maximum adsorption of the adsorbent (mg g^{-1}); K_L (L mg^{-1}), K_F (mg g^{-1} (mg L^{-1})$^{-1/nF}$), and K_g (L mg^{-1}) are the equilibrium constants for Langmuir, Freundlich, and Liu isotherm models, respectively; n_F and n_L are the dimensionless exponents for Freundlich, and Liu isotherm models, respectively.

The fitness of the kinetics and equilibrium experimental data to the nonlinear curves of the models were validated by determination of R-square, R^2 [Eq. (9)], the adjusted R-square, R^2_{adj} [Eq. (10)], and the standard deviation of residues, SD [Eq. (11)].

$$R^2 = \frac{\sum_i^n \left(q_{i,exp} - \bar{q}\exp\right)^2 - \sum_i^n \left(q_{i,exp} - q_{i,model}\right)^2}{\sum_i^n \left(q_{i,exp} - \bar{q}\exp\right)^2} \tag{9}$$

$$R^2_{adj} = 1 - \left(1 - R^2\right)\left(\frac{n-1}{n-p-1}\right) \tag{10}$$

$$SD = \sqrt{\left(\frac{1}{n-p}\right)\sum_i^n (q_{i,exp} - q_{i,model})2} \tag{11}$$

where $q_{i,exp}$ is adsorption capacity at a particular experimental; $_{exp}$ is the average of all experimental q values; $q_{i,model}$ is individual theoretical q value predicted by the model; p is the number of parameters in the fitting model; and n is the number of experiments.

Results and discussion

Characterization analysis

The UV–Visible spectra of L-Asp, uncapped Fe_3O_4 NPs, and L-Asp capped Fe_3O_4 NPs are presented in Fig. 1. L-Asp shows a strong absorption peak at 200 nm and almost zero absorbance in the rest of the region. However, both L-Asp capped and uncapped Fe_3O_4 NPs show a broad absorption peak at ∼350 nm due to the absorption and scattering of light by Fe_3O_4 NPs (Ahmad et al. 2009). The stronger absorption intensity and slight blue shift of the L-Asp capped Fe_3O_4 NPs than uncapped Fe_3O_4 NPs show the formation of Fe_3O_4 NPs by L-Asp.

The synthesis of Fe_3O_4 NPs phase was confirmed by XRD. Figure 2 shows the XRD patterns of L-Asp capped Fe_3O_4 NPs. The diffraction peaks observed at $2\theta = 18.2°$, 30.77°, 35.82°, 43.4°, 57.52°, and 63.02° are indexed to (111), (220), (311), (400), (511), and (440) diffraction planes, respectively (JCPDS, File No. 19-0629). The diffractogram confirms the formation of pure phase cubic (space group: Fd-3 m) spinel structure. A slight shift to low angle diffraction of L-Asp capped than the reference (JCPDS, File No. 19-0629) could be due to water intercalation in the layers of Fe_3O_4 NPs. Moreover, the average crystallite size of Fe_3O_4 NPs estimated using the Scherrer equation [Eq. (12)] was found to be 10 nm.

$$D = (0.9\lambda)/(\beta \cos\theta) \qquad (12)$$

where λ is the wavelength of the X-ray source ($\lambda = 0.15418$ nm), β is the peak width of the diffraction peak profile at half maximum height resulting from small crystallite size in radians, and θ is the Bragg's angle.

The capping of L-Asp and its interaction mechanism to the surface of Fe_3O_4 NPs was studied by FTIR. FTIR spectra of L-Asp, uncapped, and L-Asp capped Fe_3O_4 NPs are shown in Fig. 3. The FTIR spectrum of L-Asp shows
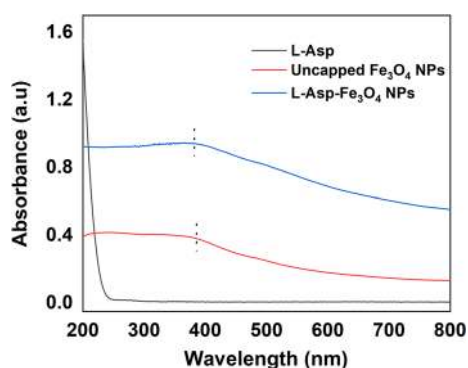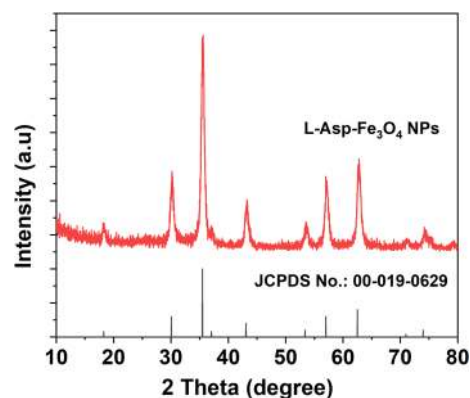

Fig. 2 The powder X-ray diffraction pattern of L-Asp capped Fe_3O_4 NPs

characteristic peaks at 3056, 1700, 1606, and 1341 cm^{-1}. The OH (intermolecular hydrogen bond) and carbonyl stretching are assigned to 3005 and 1700 cm^{-1}, respectively (Barth 2000). However, the peaks at 1606 and 1341 cm^{-1} are assigned to the asymmetric and symmetric vibrations of the carboxyl group of L-Asp, respectively (Barth 2000). Uncapped Fe_3O_4 NPs show two prominent peaks at 3427 and 1641 cm^{-1} were assigned to the O–H stretching and deforming vibration of the water molecule adsorbed on the Fe_3O_4 NPs. The peaks at 585 and 412 cm^{-1} are indexed to the intrinsic Fe–O vibrations of Fe_3O_4 NPs (Cornell and Schwertmann 2006; Mi et al. 2020). The FTIR of L-Asp capped Fe_3O_4 NPs, unlike uncapped Fe_3O_4 NPs, shows peaks at 1589, 1344, and 1117 cm^{-1} which coincides with the peak due to L-Asp. This implies the capping of Fe_3O_4 NPs by L-Asp. Besides, the mode of interaction of L-Asp onto Fe_3O_4 NPs can be derived from FTIR analysis. The energy differences between the asymmetric (1589 cm^{-1}) and symmetric (1344 cm^{-1}) stretching frequencies of carboxyl groups in L-Asp capped Fe_3O_4 give hints about the nature of

Fig. 1 The UV–Visible absorption spectra of L-Aspartic acid, uncapped Fe_3O_4 NPs, and L-Asp capped Fe_3O_4 NPs
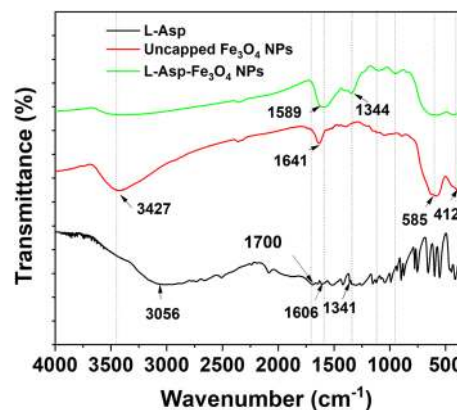

Fig. 3 The FTIR spectra of L-Aspartic acid, uncapped Fe_3O_4 NPs and L-Asp capped Fe_3O_4 NPs

the interaction of the carboxyl group with the oxide surface. Hence, the difference between the asymmetric and symmetric stretching frequencies ($\Delta\nu_{a-s} = 1589–1344 = 253$ cm^{-1}) was observed greater than 200 cm^{-1}, agreeing to the unidentate complexation of the carboxyl group with Fe$_3$O$_4$ NPs surface (Tie et al. 2006).

The surface morphology of uncapped Fe$_3$O$_4$ and L-Asp capped Fe$_3$O$_4$ NPs was investigated using SEM micrographs. Figure 4 shows the SEM images of uncapped Fe$_3$O$_4$ NPs (Fig. 4a) and L-Asp capped Fe$_3$O$_4$ NPs (Fig. 4b). The aggregation of Fe$_3$O$_4$ NPs was observed for Uncapped Fe$_3$O$_4$ NPs than the capped Fe$_3$O$_4$ NPs. Identifiable spherical nanoparticles with high surface porosity Fe$_3$O$_4$ NPs were synthesized by L-Asp. Besides, The EDS spectrum of L-Asp capped Fe$_3$O$_4$ NPs (Fig. 4c) shows the presence of C atoms, in addition to Fe and O atoms, which comes from the L-Asp. This also confirms the presence of the capping material on the surface of Fe$_3$O$_4$ NPs. The TEM images of the L-Asp capped Fe$_3$O$_4$ NPs are shown in Fig. 5. The micrograph displays the formation of uniform dispersion of spherical shape Fe$_3$O$_4$ NPs. Selected area electron diffraction (SAED) patterns obtained from the particles given in Fig. 4c are in good agreement with the characteristic electron diffraction pattern of Fe$_3$O$_4$ NPs. The mean particle size was fairly close

to the calculated crystallite size of 9.5 nm; this could be due to the majority of the observed spherical Fe$_3$O$_4$ NPs might be single crystals.

The magnetic property of L-Asp capped Fe$_3$O$_4$ NPs was measured using a vibrating sample magnetometer (VSM) at room temperature. The magnetization curve of the L-Asp capped Fe$_3$O$_4$ NPs at room temperature is depicted in Fig. 6. The superparamagnetic nature of L-Asp capped Fe$_3$O$_4$ NPs was confirmed by the absence of both coercivity and hysteresis loops without the presence of an external magnetic field. The room temperature saturation magnetization (Ms) value was 53 emu/g, which is lower than the bulk Fe$_3$O$_4$ (92 emu/g) (Wei et al. 2012; Dutta et al. 2020).

Adsorption studies

Optimization of adsorption parameters

The adsorption RhB was optimized at the different contact time, pH (2–11), and RhB concentration (5–30 mg L^{-1}) at a fixed dose of 0.1 mg mL^{-1} of Fe$_3$O$_4$ NPs and 25 °C. As it is presented in Fig. 7, the removal of RhB (5 mg L^{-1}) is highly dependent on the pH of the solution. At pH 2, the surface of L-Asp capped Fe$_3$O$_4$ NPs is positively charged (–NH$_3^+$,
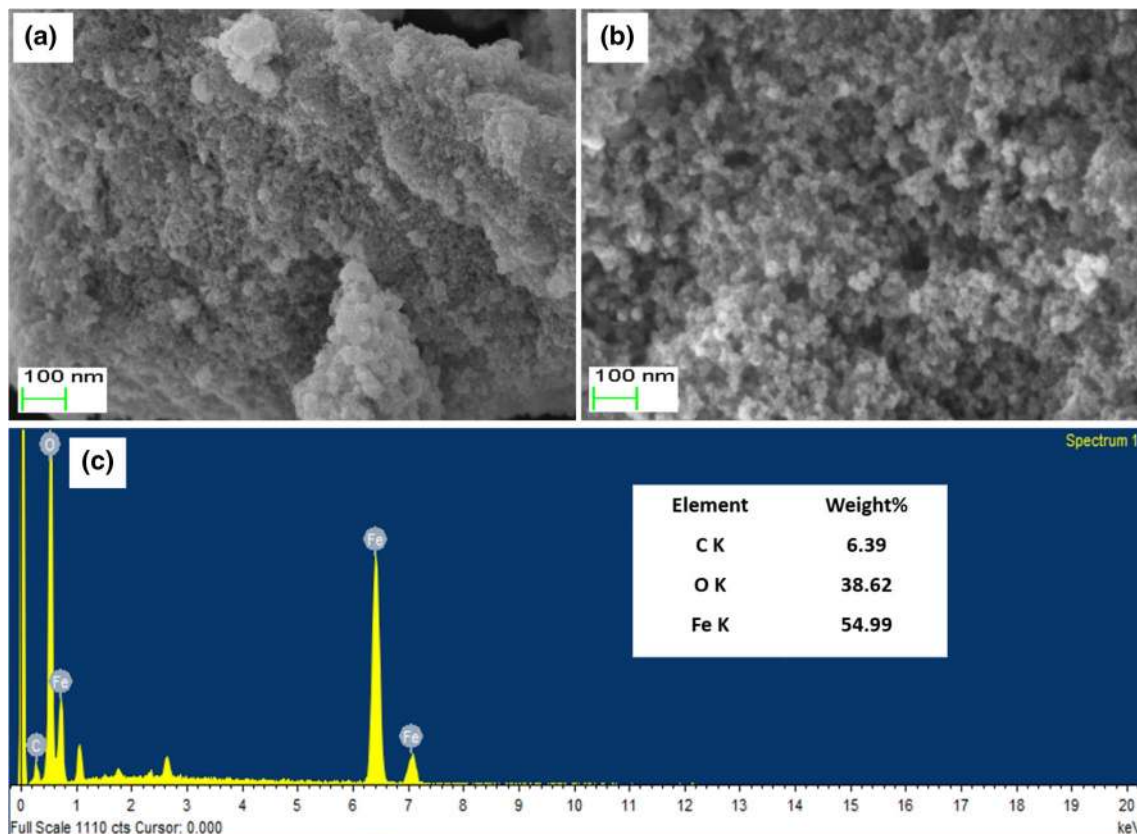

Element	Weight%
C K	6.39
O K	38.62
Fe K	54.99

Fig. 4 The representative SEM images of **a** uncapped Fe$_3$O$_4$ NPs, **b** L-Asp capped Fe$_3$O$_4$ NPs, and **c** EDS spectrum L-Asp capped Fe$_3$O$_4$ NPs
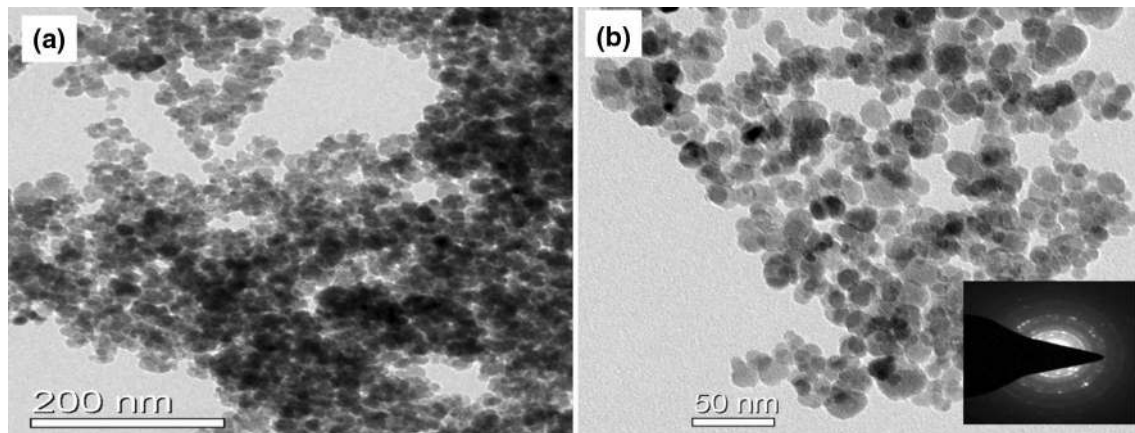
Fig. 5 The representative TEM images of L-Asp capped Fe_3O_4 NPs at different magnification scale (inset selected area electron diffraction (SAED) of L-Asp capped Fe_3O_4 NPs)
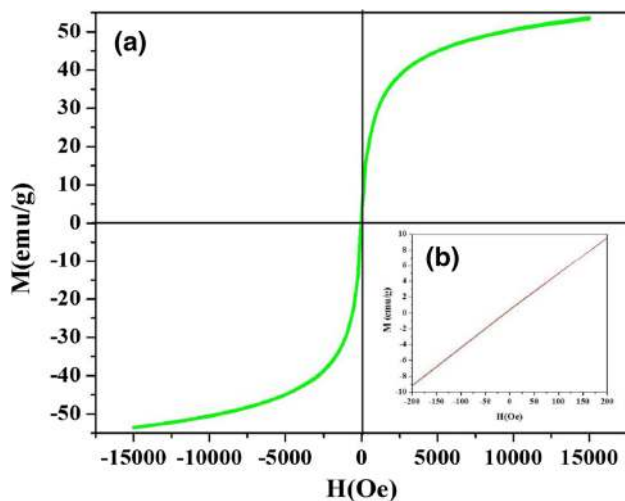

Fig. 6 a Magnetization value obtained from vibrating sample magnetometer (VSM) and **b** inset: magnified view at low H(Oe) value of L-Asp capped Fe_3O_4 NPs at room temperature

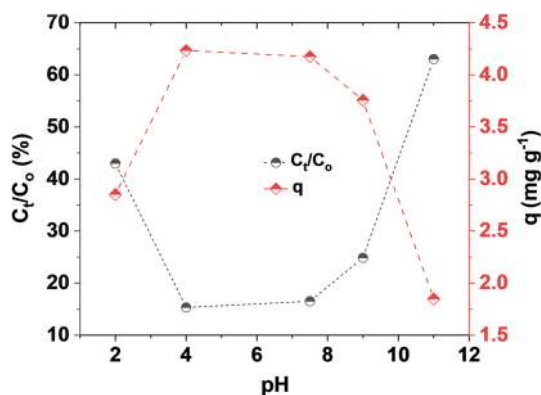**Fig. 8** The effect of contact time for adsorption of RhB (30 mg L^{-1}) onto L-Asp capped Fe_3O_4 (1 mg mL^{-1}) at pH 7 and 25 °C

Fig. 7 The effect of pH for the adsorption capacity of L-Asp capped Fe_3O_4 (1 mg mL^{-1}) to 50 mL of RhB (5 mg L^{-1}) at pH 7 and 25 °C

pH < pI = 2.77), and thus, there is an electrostatic repulsion between the L-Asp capped Fe_3O_4 NPs surface and the cationic RhB (Fig. S1). As a result, the adsorption efficiency is low (2 mg g^{-1}) at pH 2. At pH greater than the isoelectronic point of L-Asp (pH > pI = 2.77), the surface of the L-Asp capped Fe_3O_4 NPs is predominantly negatively charged and RhB is in the zwitterionic form (pKa of RhB = 3.7). This implies that the presence of strong electrostatic interaction between RhB and Fe_3O_4 surface contributes to maximum removal (4.2 mg g^{-1}) at this pH range (4–7). The amount of RhB adsorbed decreases at a pH value higher than 9, because of the electrostatic repulsion between negatively charged L-Asp capped Fe_3O_4 NPs and the zwitterionic form RhB (Fig. S2).

The rate of adsorption was investigated by taking 30 mg L^{-1} of RhB and 1 mg mL^{-1} L-Asp capped Fe_3O_4 at pH 7 and 25 °C (Fig. 8). About 70% saturation (5.4 mg g^{-1}) of the adsorption capacity was observed for the first 30 min, and then, the adsorption process continued slowly to reach
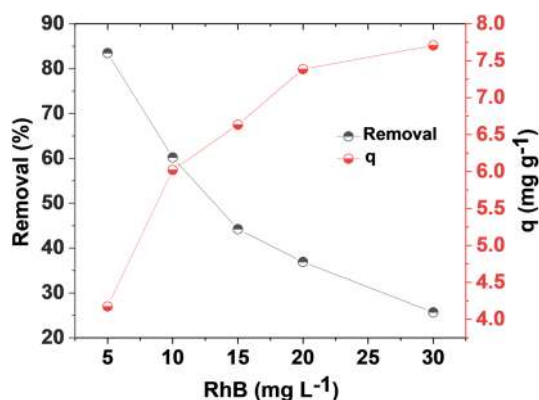
Fig. 9 The effect of RhB concentrations (5–30 mg L^{-1}) for the adsorption capacity L-Asp capped Fe_3O_4 (1 mg mL^{-1}) at pH 7 and 25 °C
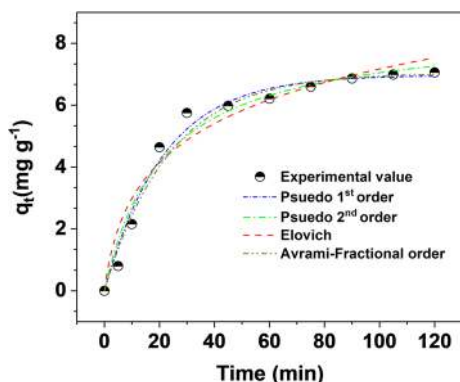

Fig. 10 The adsorption kinetics plots for the removal of 30 mg L^{-1} RhB (50 mL) by L-Asp capped Fe_3O_4 (1 mg mL^{-1}) at pH 7 and 25 °C

the equilibrium (7.7 mg g^{-1}) at 180 min. Figure 9 shows the adsorption efficiency of L-Asp capped Fe_3O_4 at varying initial concentrations of RhB. The adsorption capacity (q) increases with RhB concentration, but the removal (%) of RhB is the reversal.

Adsorption kinetics analysis

The kinetics of RhB adsorption is investigated by the nonlinear fitting of pseudo-first-order, pseudo-second-order, Avrami-Fractional-order, and Elovich model models (Fig. 10). Table 1 summarizes all the kinetics parameters derived from all models. The analysis was assessed by using 0.1 mg mL^{-1} of Fe_3O_4 NPs and 50 ml of RhB (30 mg L^{-1}) at varying contact time. The correlation coefficient (R^2_{adj}) and standard deviation, SD (mg g^{-1}) statistical values were used to evaluate the best fitting model. The Avrami fractional order has the highest R^2adj (0.99) and the lowest SD (0.32974) than others. This seems that the kinetics process of RhB adsorption onto Fe_3O_4 was reasonably interpreted by Avrami fractional order.

Adsorption isotherm analysis

The equilibrium adsorption phenomenon of RhB adsorption onto L-Asp capped Fe_3O_4 NPs was assessed by the Langmuir, Freundlich, and Liu models. The isotherm plots and derived parameters are presented in Fig. 11 and Table 2, respectively. The Liu model based on R^2 (0.984) and lowest SD (0.171) values is selected as the best model to evaluate the equilibrium process. The maximum theoretical adsorption capacity (Q_o) of L-Asp capped Fe_3O_4 NPs was predicted to 10.44 mg L^{-1}. The L-Asp capped Fe_3O_4 NPs show a competitive efficiency to the reported adsorbent materials used for RhB removal (Table S1).

Recoverability of L-Asp-Fe_3O_4 NPs

The recoverability test is a prime concern for the practical application of adsorbents. Five successive cycles of adsorptions of RhB were carried out to evaluate the recoverability of L-Asp-Fe_3O_4 NPs. The condition for optimum removal efficiency (1 mg mL^{-1} adsorbent, and 30 mg L^{-1} RhB at pH

Table 1 The kinetics parameters obtained from the adsorption RhB onto L-Asp capped Fe_3O_4 NPs (1 mg mL^{-1})

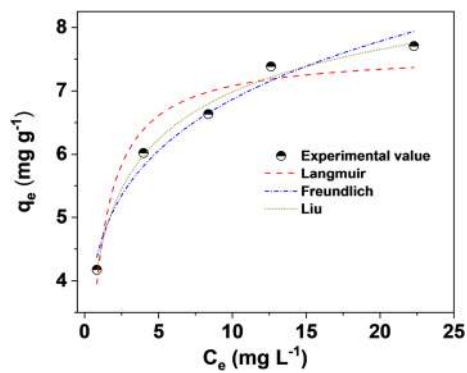| Pseudo-first order	Pseudo-second order	Avrami fractional-order	Elovich model
k_1 (min^{-1}) = 0.036	k_2 (g mg^{-1} min^{-1}) = 0.0055	k_{AV} (min^{-1}) = 0.059 n_{AV} = 0.594	a (g mg^{-1}) = 0.391
q_e (mg g^{-1}) = 7.4	q_e (mg g^{-1}) = 8.54	q_e (mg g^{-1}) = 7.65	b (mg g^{-1} min^{-1}) = 0.457
R^2_{adj} = 0.98	R^2_{adj} = 0.968	R^2_{adj} = 0.99	R^2_{adj} = 0.959
SD (mg g^{-1}) = 0.33965	SD (mg g^{-1}) = 0.4534	SD (mg g^{-1}) = 0.32974	SD (mg g^{-1}) = 0.57425

Fig. 11 The equilibrium adsorption isotherm curves for 30 mg/L RhB (50 mL) adsorbed on L-Asp capped Fe_3O_4 (1 mg/mL) at pH 7 and 25 °C
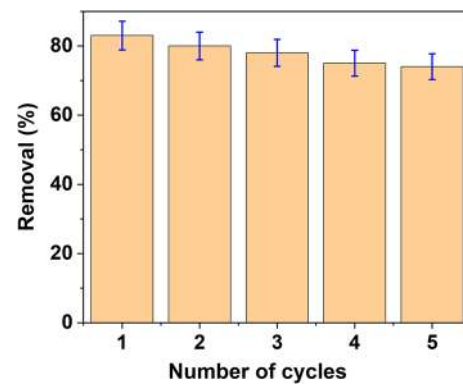

Fig. 12 The recyclability of the L-Asp capped Fe_3O_4 NPs (1 mg mL^{-1}) for the removal of RhB (5 mg L^{-1}) within 5 successive runs. (Error bar represents 5% error)

Table 2 The isotherm parameters obtained from the adsorption of RhB onto L-Asp capped Fe_3O_4 NPs (1 mg mL^{-1})

Langmuir	Freundlich	Liu
Q_{max} (mg g^{-1}) = 7.62	K_F (mg g^{-1} (mg L^{-1})$^{-1/nF}$) = 4.53	Q_{max} (mg g^{-1}) = 10.44
K_L (L mg^{-1}) = 1.31	n_F = 5.534	K_g (L mg^{-1}) = 0.48632
R^2adj = 0.92	R^2adj = 0.968	n = 0.4441
SD (mg g^{-1}) = 0.39237	SD (mg g^{-1}) = 0.249	R^2adj = 0.984
		SD (mg g^{-1}) = 0.171

7 and 25 °C) was used for the recoverability test. After each consecutive cycle, the L-Asp-Fe_3O_4 NPs were collected, washed at least three times, and dried in the oven for further use. As it is shown in Fig. 12, within a 5% error, the L-Asp-Fe_3O_4 NPs were successfully reused for five successive adsorption cycles. This indicates the potential of L-Asp-Fe_3O_4 NPs reusability for the successive experiments.

Conclusion

In conclusion, we have synthesized Fe_3O_4 NPs using amino acid as an environmentally benign capping agent. Highly crystalline, pure phase, superparamagnetic, and a homogeneous spherical Fe_3O_4 NPs formation were examined by advanced analytical instrumentation. The adsorptive removal efficiency of L-Asp capped Fe_3O_4 NPs was evaluated using RhB as a model dye. The optimum adsorption efficiency was found to be 7.7 mg g^{-1} at 1 mg mL^{-1} of Fe_3O_4 NPs, 30 mg L^{-1} RhB, pH 7, and 25 °C. The kinetics of the adsorptive removal of L-Asp capped Fe_3O_4 NPs toward RhB had followed Avrami fractional order. The equilibrium adsorption process is sufficiently explained by Liu isotherm model. The maximum adsorption based on Liu isotherm model was predicated to 10.44 mg g^{-1}. This implies that the L-Asp capped Fe_3O_4 NPs is a promising competitive adsorbent for the removal of RhB.

Compliance with ethical standards

Conflict of interest The authors declare that they have no conflict of interest.

References

Ahmad S, Riaz U, Kaushik A, Alam J (2009) Soft template synthesis of super paramagnetic Fe_3O_4 nanoparticles a novel technique. J Inorg Organomet Polym Mater 19:355–360

Alkaykh S, Mbarek A, Ali-Shattle EE (2020) Photocatalytic degradation of methylene blue dye in aqueous solution by $MnTiO_3$ nanoparticles under sunlight irradiation. Heliyon 6:e03663

Amin MT, Alazba AA, Manzoor U (2014) A review of removal of pollutants from water/wastewater using different types of nanomaterials. Adv Mater Sci Eng 2014:1–24

Anjum M, Miandad R, Waqas M et al (2019) Remediation of wastewater using various nano-materials. Arab J Chem 12:4897–4919

Anwer H, Mahmood A, Lee J et al (2019) Photocatalysts for degradation of dyes in industrial effluents: opportunities and challenges. Nano Res 12:955–972

Barth A (2000) The infrared absorption of amino acid side chains. Prog Biophys Mol Biol 74:141–173

Belachew N, Bekele G (2020) Synergy of magnetite intercalated bentonite for enhanced adsorption of congo red dye. Silicon 12:603–612

Belachew N, Kahsay MH, Tadesse A, Basavaiah K (2020) Green synthesis of reduced graphene oxide grafted Ag/ZnO for photocatalytic abatement of methylene blue and antibacterial activities. J Environ Chem Eng 8:104106

Belachew N, Rama Devi D, Basavaiah K (2017) Green synthesis and characterisation of L-Serine capped magnetite nanoparticles for removal of Rhodamine B from contaminated water. J Exp Nanosci 12:114–128

Belachew N, Rama Devi D, Basavaiah K (2016) Facile green synthesis of l-methionine capped magnetite nanoparticles for adsorption of pollutant Rhodamine B. J Mol Liq 224:713–720

Burakov AE, Galunin EV, Burakova IV et al (2018) Adsorption of heavy metals on conventional and nanostructured materials for wastewater treatment purposes: a review. Ecotoxicol Environ Saf 148:702–712

Chieng HI, Lim LBL, Priyantha N (2015) Sorption characteristics of peat from Brunei Darussalam for the removal of rhodamine B dye from aqueous solution: adsorption isotherms, thermodynamics, kinetics and regeneration studies. Desal. Water Treat. 55:664–677

Cornell RM, Schwertmann U (2006) The iron oxides: structure, properties, reactions, occurrences and uses. Wiley, New York

Dotto GL, McKay G (2020) Current scenario and challenges in adsorption for water treatment. J Environ Chem Eng 8:103988

Dutta B, Nema A, Shetake NG et al (2020) Glutamic acid-coated Fe3O4 nanoparticles for tumor-targeted imaging and therapeutics. Mater Sci Eng, C 112:110915

Gao F (2019) An overview of surface-functionalized magnetic nanoparticles: preparation and application for wastewater treatment. Chem Select 4:6805–6811

Gupta NK, Ghaffari Y, Kim S, et al (2020) Photocatalytic degradation of organic pollutants over MFe2O4 (M = Co, Ni, Cu, Zn) Nanoparticles at neutral pH. Scientific reports no. 10

Gutierrez AM, Dziubla TD, Hilt JZ (2017) Recent advances on iron oxide magnetic nanoparticles as sorbents of organic pollutants in water and wastewater treatment. Rev Environ Health 32:111–117

Kahsay MH, Tadesse A, RamaDevi D et al (2019) Green synthesis of zinc oxide nanostructures and investigation of their photocatalytic and bactericidal applications. RSC Adv 9:36967–36981

Kausar A, Iqbal M, Javed A et al (2018) Dyes adsorption using clay and modified clay: a review. J Mol Liq 256:395–407

Keyhanian F, Shariati S, Faraji M, Hesabi M (2016) Magnetite nanoparticles with surface modification for removal of methyl violet from aqueous solutions. Arab J Chem 9:S348–S354

Kiwaan HA, Atwee TM, Azab EA, El-Bindary AA (2020) Photocatalytic degradation of organic dyes in the presence of nanostructured titanium dioxide. J Mol Struct 1200:127115

Kooh MRR, Dahri MK, Lim LBL (2016) The removal of rhodamine B dye from aqueous solution using *Casuarina equisetifolia* needles as adsorbent. Cogent Environ Sci 2:1140553

Lakouraj MM, Norouzian R-S, Balo S (2015) Preparation and cationic dye adsorption of novel fe3o4 supermagnetic/thiacalix[4] arene tetrasulfonate self-doped/polyaniline nanocomposite: kinetics, isotherms, and thermodynamic study. J Chem Eng Data 60:2262–2272

Majid Z, AbdulRazak AA, Noori WAH (2019) Modification of zeolite by magnetic nanoparticles for organic dye removal. Arab J Sci Eng 44:5457–5474

Mi T, Cai Y, Wang Q et al (2020) Synthesis of Fe3O4 nanocomposites for efficient separation of ultra-small oil droplets from hexadecane–water emulsions. RSC Adv 10:10309–10314

Mohanraj J, Durgalakshmi D, Balakumar S et al (2020) Low cost and quick time absorption of organic dye pollutants under ambient condition using partially exfoliated graphite. J Water Process Eng 34:101078

Nosrati H, Salehiabar M, Bagheri Z et al (2018) Preparation, characterization, and evaluation of amino acid modified magnetic nanoparticles: drug delivery and MRI contrast agent applications. Pharm Dev Technol 23:1156–1167

Rajasulochana P, Preethy V (2016) Comparison on efficiency of various techniques in treatment of waste and sewage water—a comprehensive review. Resour-Effi Technol 2:175–184

Schwaminger SP, García PF, Merck GK et al (2015) Nature of interactions of amino acids with bare magnetite nanoparticles. J Phys Chem C 119:23032–23041

Sellaoui L, Lima EC, Dotto GL, Ben Lamine A (2017) Adsorption of amoxicillin and paracetamol on modified activated carbons: equilibrium and positional entropy studies. J Mol Liq 234:375–381

Shan J, Wang L, Yu H-J et al (2015) Synthesis and characterization of magnetic porous Fe_3O_4/poly(methylmethacrylate-co-divinylbenzene) microspheres and their use in removal of Rhodamine B. J Zhejiang Univ-Sci A 16:669–679

Singh S, Kumar A, Gupta H (2020) Activated banana peel carbon: a potential adsorbent for Rhodamine B decontamination from aqueous system. Appl Water Sci 10:1–8

Tie S-L, Lin Y-Q, Lee H-C et al (2006) Amino acid-coated nano-sized magnetite particles prepared by two-step transformation. Coll Surf, A 273:75–83

Wei Y, Han B, Hu X et al (2012) Synthesis of Fe_3O_4 nanoparticles and their magnetic properties. Proced Eng 27:632–637